Monthly Notices
of the
ROYAL ASTRONOMICAL SOCIETY

MNRAS **472,** 3277–3287 (2017)
Advance Access publication 2017 July 19

doi:10.1093/mnras/stx1816

The magnetic field inside a protoplanetary disc gap opened by planets of different masses

Augusto Carballido,★ Lorin S. Matthews★ and Truell W. Hyde

Center for Astrophysics, Space Physics and Engineering Research, Baylor University, Waco, TX 76798, USA

Accepted 2017 July 15. Received 2017 July 14; in original form 2017 February 22

ABSTRACT

We perform magnetohydrodynamic simulations of protoplanetary disc gaps opened by planets of various masses, with the aim of calculating the strength of the vertical magnetic field threading such gaps. We introduce a gravitational potential at the centre of a shearing box to compute the tidal interaction between the planets and the disc gas, which is turbulent due to the magnetorotational instability. Two types of simulations are executed: 1) In type 'Z', the initial magnetic field has only a uniform, vertical component, and ten planet masses between 0.66 and 6.64 thermal masses are used; 2) In type 'YZ', the initial magnetic field has both toroidal and vertical components, and five planet masses covering the same mass range are used. Our results show that, for low planet masses, higher values of the vertical magnetic field occur inside the gaps than outside, in agreement with the previous work. However, for massive planets, we find that the radial profiles of the field show dips near the gap centre. The interior of the Hill sphere of the most massive planet in the Z runs contains more low-plasma β values (i.e. high magnetic pressure) compared to lower-mass planets. Values of β at a distance of one Hill radius from each planet show a moderate decrease with planet mass. These results are relevant for the magnetic structure of circumplanetary discs and their possible outflows, and may be refined to aid future observational efforts to infer planet masses from high-resolution polarimetric observations of discs with gaps.

Key words: MHD – methods: numerical – planet–disc interactions – protoplanetary discs.

1 INTRODUCTION

The spectacular discovery of annular gaps and bright rings in protoplanetary discs (PPDs; ALMA Partnership et al. 2015; Akiyama et al. 2015; van Boekel et al. 2017) has led to an increased interest in understanding the origin and evolution of such sub-structures (Dong et al. 2011; Gressel et al. 2013; Zhu, Stone & Rafikov 2013; Fung & Chiang 2016). Various mechanisms have been proposed to explain the presence of these axisymmetric features, as found, for example in the discs around TW Hya and HL Tau. Re-condensation of ice near condensation fronts could modify the opacity due to solids, potentially explaining the concentric bright and dark rings that are revealed by the 870 μm continuum emission from the TW Hya disc (Andrews et al. 2016). In the specific case of dark gaps, it has been shown that the tidal interaction between planetary-mass objects and the host disc could decrease the gas density enough to produce these observed features. This dynamical mechanism is well understood (Kley & Nelson 2012), with gap opening recognized as closely linked to Type II planetary migration (Lin & Papaloizou 1986).

Theoretical studies of the conditions found inside PPD gaps point to an active magnetohydrodynamic (MHD) environment. Papaloizou, Nelson & Snellgrove (2004) found that both global and local ideal-MHD simulations of protoplanets interacting with an MHD-turbulent disc exhibited similar gap features. In particular, in both types of simulations, the magnetic field strength increased near the spiral shock waves generated by the protoplanet but, on average, the magnetic energy density decreased inside the gap. Likewise, in both cases the magnetic field was advected into the protoplanetary Hill sphere, creating fluid circulation about the protoplanet that could lead to the possibility of magnetic braking of the circumplanetary disc (CPD), in turn leading to enhanced accretion of material on to the protoplanet compared to non-magnetized discs.

Local MHD simulations of gap opening by low-mass planets have shown that vertical magnetic fields tend to be strong inside the gap (Zhu et al. 2013). This result, obtained in the ideal-MHD regime, has important implications for the dynamics of CPDs since the availability of vertical fields is crucial for the development of the magnetorotational instability (MRI) in such systems (Fujii et al. 2014;

★ E-mail: Augusto_Carballido@baylor.edu (AC); Lorin_Matthews@baylor.edu (LSM)

Keith & Wardle 2014; Turner et al. 2014). In turn, the presence or absence of MRI turbulence in CPDs has a bearing on the radial distribution of the chemical species in these discs, as well as on the composition of any satellites formed.

Using global simulations of a planet embedded in a magnetically inactive dead zone, generated by the presence of Ohmic resistivity, Gressel et al. (2013) showed that the gap opening process can actually lead to the development of MRI turbulence in the vicinity of the planet, since stellar X-rays and cosmic rays are both able to penetrate the gap region increasing the ionization fraction and facilitate the onset of the MRI. The accretion of material into the gap and the planet's Hill sphere occurs mostly from the magnetically active surface layers of the host PPD. This process drags magnetic fields which can enter the rotating CPD, possibly contributing to the launch of magnetically driven outflows.

The role of non-ideal MHD effects in the structure of the magnetic field across a gap opened by a Jupiter-mass planet was recently examined in detail by Keith & Wardle (2015). Using data from a snapshot produced by a purely hydrodynamical, gap-opening simulation by Tanigawa, Ohtsuki & Machida (2012) and Keith & Wardle (2015) confirmed that a magnetic field would be easily drawn into the gap and circumplanetary disc. This field would be mostly toroidal, but its vertical component could determine the susceptibility of the flow to MRI turbulence close to the mid-plane, depending on the relative orientation between the vertical field and the disc's angular momentum vector.

While previous studies generally agree that magnetic fields are easily transported into the gap region, they have been conducted for only a limited number of planetary masses. During the course of a previous study of gap opening by a planet approximately twice as massive as Jupiter (Carballido, Matthews & Hyde 2016), we noticed that the radial profile of the magnetic field across the gap differed considerably from that reported by Zhu et al. (2013) for a lower-mass planet. Therefore, the goal of this paper is to obtain a better understanding of the possible values of the gap magnetic field (GMF) by expanding the parameter space corresponding to the planet mass. Similarly, we wish to determine if the initial configuration of the magnetic field has an effect on the value of the GMF, since it has been shown that the initial field geometry is crucial for the evolution of the MHD flow in disc simulations (Turner et al. 2014). We will assume ideal-MHD conditions throughout this work. The prevailing view in the literature is that MRI turbulence occurs high in the disc atmosphere, within a few tenths of an AU of the central star, and beyond several tens of AU, all of which are locations where ionization is effective. The disc interior, however, is likely to be much less turbulent (Turner et al. 2014; Armitage 2015). The justification for our assumption of ideal MHD comes from the results by Keith & Wardle (2015), who found that, even in the presence of non-ideal MHD effects, one of these, the Hall effect, can destabilize the flow and enhance turbulence if sign $(\mathbf{B}\cdot\mathbf{\Omega})=\mathbf{1}$, where $\mathbf{B}$ and $\mathbf{\Omega}$ are the magnetic field and the disc angular velocity vectors, respectively. In that case, the resulting MRI-unstable flow is important not only in regions above half a scale height in protostellar discs in which a planet has opened a gap, but also close to the midplane [see, for example, Fig. 3 of Keith & Wardle (2015)]. We expect this study will serve as a first step towards elucidating the masses of gap-opening planets from the observed properties of the GMF, obtained when polarimetric observations reach a sufficient spatial resolution.

Our paper is structured as follows. Section 2 describes our numerical models of planet-induced gap opening in a PPD with a magnetohydrodynamic flow, as well as the set-up of the initial and boundary conditions. Section 3 presents the outcome of a total of 15 simulations of gap opening by planets of different masses. These simulations are divided into two groups, corresponding to two different initial magnetic field configurations. In Section 4, we discuss our results and some implications for gap processes, and a summary of our conclusions is given in Section 5.

2 METHOD

2.1 Disc and planet models

Our local model of a PPD consists of a rectangular box divided into identical cells, in which the relevant physical variables are evaluated, stored and updated. The ATHENA code (Stone et al. 2008) is used to solve the MHD equations in the shearing box approximation (Hawley, Gammie & Balbus 1995). The rectangular coordinate system associated with the box corotates with the disc at a fiducial orbital radius R_0 and angular frequency $\Omega_0=\Omega(R_0)$. The x-axis is oriented along the disc's radial direction, the y-axis along the azimuthal direction (neglecting the disc's curvature) and the z-axis is parallel to the angular velocity vector Ω. The differential rotation of the PPD is modelled as a shear flow. The boundary conditions are periodic along the three spatial directions, except that when a parcel of fluid exits one of the two radial (x) walls, it reappears through the opposite wall with a different azimuthal (y) position and velocity, given by the shearing motion.

We follow the numerical set-up of Zhu et al. (2013): The box dimensions are $16\,H\times16\,H\times H$, where H is the disc scaleheight, and with a spatial resolution of 32 grid cells per H. The gas sound speed c_s, the initial gas density ρ_0 and the angular frequency Ω_0 are all set equal to 1 in the code's system of units. The disc is isothermal, and we do not include the vertical stratification that would arise as a result of the vertical component of the central star's gravitational field.

We employ two initial magnetic field configurations: a uniform, purely vertical field and a field with both toroidal and vertical components. In both configurations, the initial field strength is given by the initial plasma beta, β_0 (the ratio of gas pressure P_0 to magnetic pressure $B_{z0}^2/8\pi$, the latter given by the vertical component of the field, B_{z0}), which is set to 400.

The gravitational effect of a planet on the surrounding disk gas is modeled by a cylindrical potential located at the box center, with the cylindrical axis coinciding with the box's vertical axis. The planet potential is given by

$$\Phi_p=-GM_p\frac{r^2+1.5r_s^2}{\left(r^2+r_s^2\right)^{3/2}},\tag{1}$$

where G is the gravitational constant, M_p is the planet mass, r is the distance to the z axis, and r_s is a smoothing length to avoid small time steps close to the source. As in Zhu et al. (2013), this smoothing length is chosen so that the free-fall timescale on to the planet, given by (Dong et al. 2011)

$$t_{ff}\approx\left(\frac{0.8r_s^3}{GM_p}\right)^{1/2}\tag{2}$$

is equal to 0.125. This value ensures that the numerical time step is $dt\lesssim t_{ff}/100$, a requirement to resolve the fluid motion around the planet.

The potential in Eq. (1) is preferred over the more commonly used second-order-accurate potential $\Phi_p^{(2)}=-GM_p/\left(r^2+r_s^2\right)^{1/2}$, because the former agrees with the Newtonian potential

Table 1. Simulation properties.

Run	Planet mass M_p		Run time (Orbits)	Initial magnetic field geometry
	M_{th}	M_J (MMSN at 3 au)		
Z1	0.66	0.23	300	Vertical
Z2	1.33	0.46	300	Vertical
Z3	1.99	0.69	300	Vertical
Z4	2.66	0.92	300	Vertical
Z5	3.32	1.15	222	Vertical
Z6	3.98	1.38	264	Vertical
Z7	4.65	1.61	238	Vertical
Z8	5.31	1.84	211	Vertical
Z9	5.98	2.07	200	Vertical
Z10	6.64	2.30	300	Vertical
YZ1	0.66	0.23	300	Toroidal + Vertical
YZ2	1.66	0.57	300	Toroidal + Vertical
YZ3	3.32	1.15	290	Toroidal + Vertical
YZ4	4.98	1.72	113	Toroidal + Vertical
YZ5	6.64	2.30	123	Toroidal + Vertical

$\Phi = -GM_p/r$ within 1% accuracy at distances as small as $2.3r_s$ from the planet, whereas the latter achieves this agreement only at a distance of $7r_s$ (Dong et al. 2011). Our chosen potential is also smoothed to take into account discontinuities at the box boundaries:

$$\Phi_{p,s}(r) = \begin{cases} \Phi_p(r_f) - \sqrt{\left[\Phi_p(r_f) - \Phi_p(r)\right]^2 + G^2 M_p^2/r_{co}^2}, & \text{if } r < r_f \\ \Phi_p(r_f) - GM_p/r_{co}, & \text{if } r > r_f \end{cases} \quad (3)$$

where r_f is the cutoff distance from the z axis beyond which the potential flattens out, and r_{co} is a smoothing length at the cutoff radius. Following Zhu et al. (2013), we set $r_f = 7.5H$ and $r_{co} = 50H$.

We express the planet mass in Eq. (1) in terms of the thermal mass $M_{th} = c_s^3/(G\Omega)$, defined as the mass at which the Hill radius and the Bondi radius of the planet are comparable to the disk scale height (Rafikov 2006; Dong et al. 2011). In the context of the minimum-mass solar nebula model (MMSN; Hayashi (1981)), for a solar-mass central star, the thermal mass can be expressed as (Dong et al. 2011):

$$M_{th} \approx 0.038 \left(\frac{c_s}{1\ \text{km s}^{-1}}\right)^3 \left(\frac{R_p}{1\ \text{AU}}\right)^{3/2} M_J, \quad (4)$$

where c_s is the sound speed in the disk, R_p is the semi-major axis of the planet's orbit, and M_J is the mass of Jupiter.

Zhu et al. (2013) examined three planet masses in their study: $M_p = 0.1, 0.3$ and $1M_{th}$. We build upon their work by extending the number of planet masses investigated, with a particular emphasis on higher mass values. The new planet masses are listed in Table 1.

2.2 Simulations

Table 1 lists the simulations that were performed. In column 1, each simulation is labelled with either 'Z', to indicate an initially vertical, uniform magnetic field $\mathbf{B}_0 = (0, 0, B_{z0})$, or 'YZ', to denote an initial field with both vertical and toroidal components, $\mathbf{B}_0 = (0, B_{y0}, B_{z0})$, with $B_{y0} = B_{z0} = \sqrt{P_0/\beta_0}$. Also shown are the corresponding planet masses, both in terms of the thermal mass (column 2) and an equivalent fraction of the Jupiter mass in the MMSN, at an orbital radius of 3 au, calculated from equation (3) (column 3). The duration of each run is shown in column 4.

We begin with a single simulation without a planet potential, to allow the MRI to develop and the disc gas to reach a turbulent state. This occurs after ∼4 orbits (where the period of one orbit is $2\pi/\Omega_0$). The simulation is allowed to progress until orbit 10, at which point the planet potential given by equation (1) is introduced. The system is then allowed to evolve thereafter and to reach a steady state, which can be corroborated by plotting the time histories of the volume-averaged turbulent parameter α (Shakura & Sunyaev 1973; Balbus & Hawley 1998), given by

$$\alpha = \frac{w_{xy}}{P}, \quad (5)$$

where P is the gas pressure and w_{xy} is the x–y component of the stress tensor, given in turn by the sum of magnetic and hydrodynamic stresses

$$w_{xy} = -\frac{B_x B_y}{4\pi} + \rho v_x \delta v_y, \quad (6)$$

with B_x and v_x the radial components of the magnetic field and the gas velocity, respectively, and δv_y the toroidal component of the turbulent gas velocity (i.e. with the background shear removed).

Fig. 1 shows a sample of time histories of α starting at $t = 10$ orbits, corresponding to runs Z1, Z5 and Z10 (three upper curves), as well as to runs YZ1, YZ3 and YZ5 (three lower curves, whose values have been divided by two to avoid an overlap with the top curves). It is evident that a steady state has been reached. For the purpose of carrying out time averages of different quantities during our data analysis, we use the last 50 orbits of each run.

3 RESULTS

The conditions associated with gaps opened by planets can be characterized by the gas density ρ, the plasma β, the turbulent parameter α and the vertical field strength B_z. We now look at our simulation results for these quantities.

3.1 Gas density and plasma β

Fig. 2 shows a snapshot of the gas density (ρ, left-hand panel) and plasma β (right-hand panel) at 46 orbits into the evolution of Run Z1, which corresponds to the smallest planet of mass $M_p = 0.66M_{th}$. Both ρ and β have been averaged over the height of the box. The black circle has a radius equal to the planet's Hill radius, R_H. A gap has been cleared by the planet and the smaller values of β (corresponding to high values of the vertical magnetic field and shown in dark colours on the right-hand panel of Fig. 2) are already more concentrated in the gap region than outside it.

A similar situation arises in the case of a mid-sized planet, run Z5 ($M_p = 3.32M_{th}$), as shown in Fig. 3. A rough correspondence can be seen between low-β regions and the high-density planetary wake that trails away from the planet (such wakes occur at locations where a strong wave is sent out from the planet into the shearing flow; Papaloizou et al. 2004). More precisely, in this snapshot, the low-β values occur on the inside of the wakes.

The largest accumulation of low-β regions inside the gap occurs for the largest planet, shown in run Z10 ($M_p = 6.64M_{th}$) in Fig. 4. This accumulation takes place within a band ∼$4H$ wide, narrower than the density gap, which is ∼$8H$ in width. There is no noticeable correspondence between the planetary wake and particular values of β. Interestingly, the region inside the planet's Hill sphere (HS) contains a significant amount of medium-β gas, or weaker magnetic fields. In Figs 5–7, we show similar maps to those of Figs 2–4, but

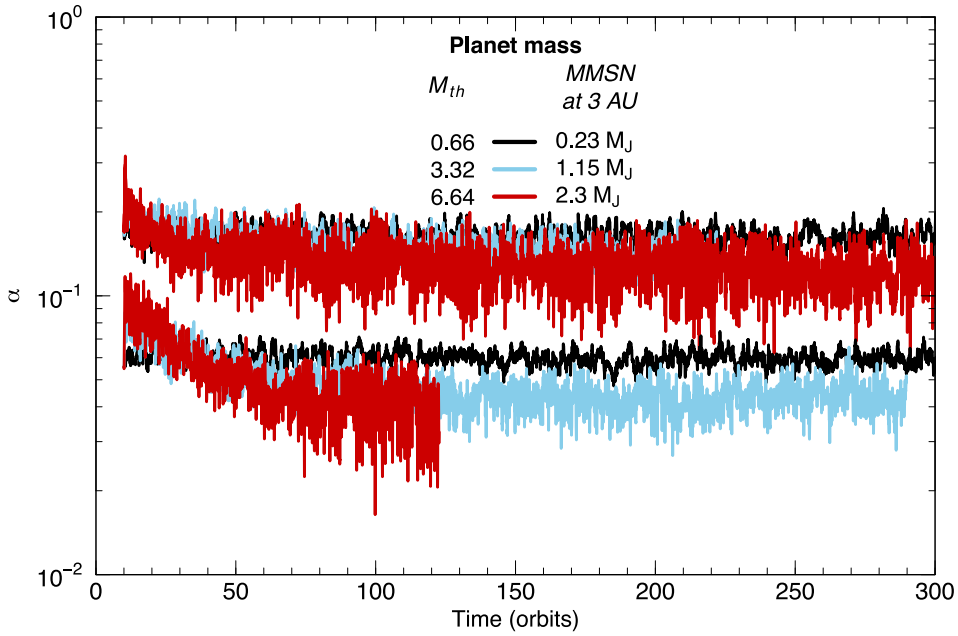

Figure 1. Time history of the volume-averaged α parameter, given by equation (4), for runs Z1 (upper black curve), Z5 (upper blue curve) and Z10 (upper red curve), and for runs YZ1 (lower black curve), YZ3 (lower blue curve) and YZ5 (lower red curve). Values of the YZ curves have been divided by 2 to avoid an overlap with the Z curves.

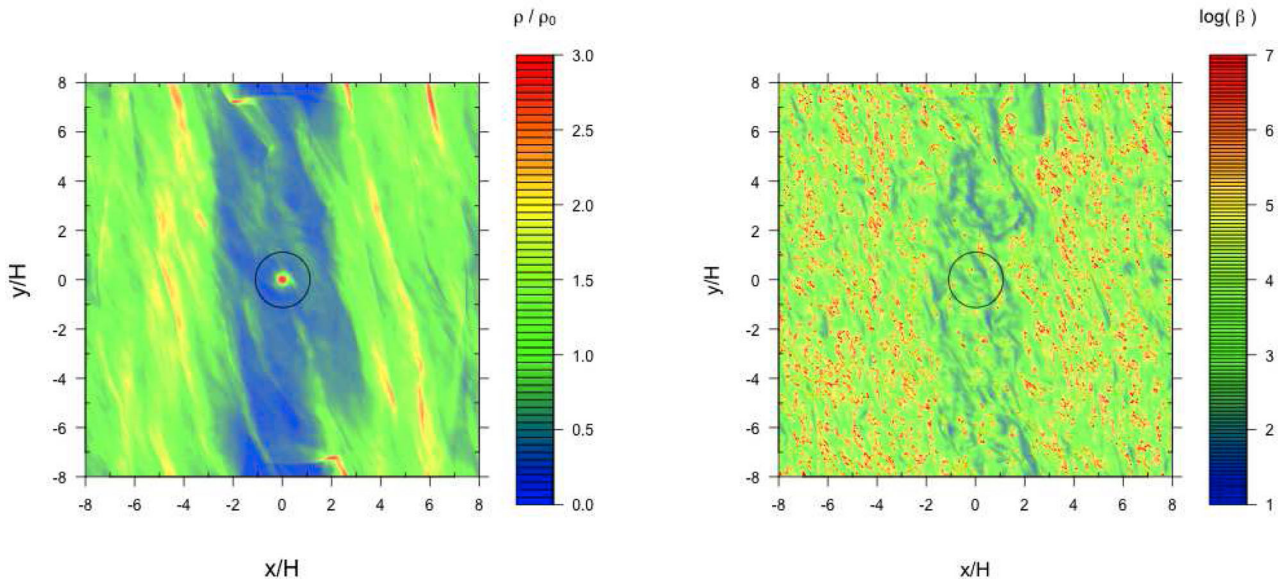

Figure 2. Vertically averaged gas density (left-hand panel) and plasma β (right-hand panel) after 46.4 orbits of evolution of run Z1, in which the planet mass is $M_p = 0.66 M_{th}$. Regions in which β is low (or equivalently, where the vertical magnetic field is high) are clustered inside the gap. The black circle represents the 'surface' of the planet's Hill sphere.

using time-averaged data. In this case, high-β regions are more concentrated outside the gap compared to the single-snapshot case. In Fig. 7, one can also discern a slight correspondence between some low-β regions and the high-density wakes, where again the regions of low β occur inside the wakes. Overall, the time-averaged β maps confirm that stronger vertical magnetic fields tend to concentrate within a strip inside the gap.

This is quantified in Fig. 8, in which we plot the distribution of β values inside the HS of the planets shown in Figs 2–7. These distributions are taken over the computational grid cells enclosed by the respective HS (after the vertical averaging), and have been averaged over time as indicated in Section 2.2. The value of β within a planet's Hill sphere is of interest as it has a direct bearing on the possibility that a CPD may develop turbulence, perhaps driving planet growth through accretion of disc material.

For the three planet masses sampled in both the Z and the YZ runs, most of the β values within the HS are $\gtrsim 10^3$. Only in the case of the most massive planet of the Z runs (red histogram in Fig. 8a) do we count ∼20 per cent of the grid points inside the HS having $\beta \lesssim 10^3$, with some β values as low as ∼10. In the case of the mid-mass and high-mass planets that correspond to runs YZ3 and YZ5, respectively (blue and red histograms in Fig. 8b), the lowest

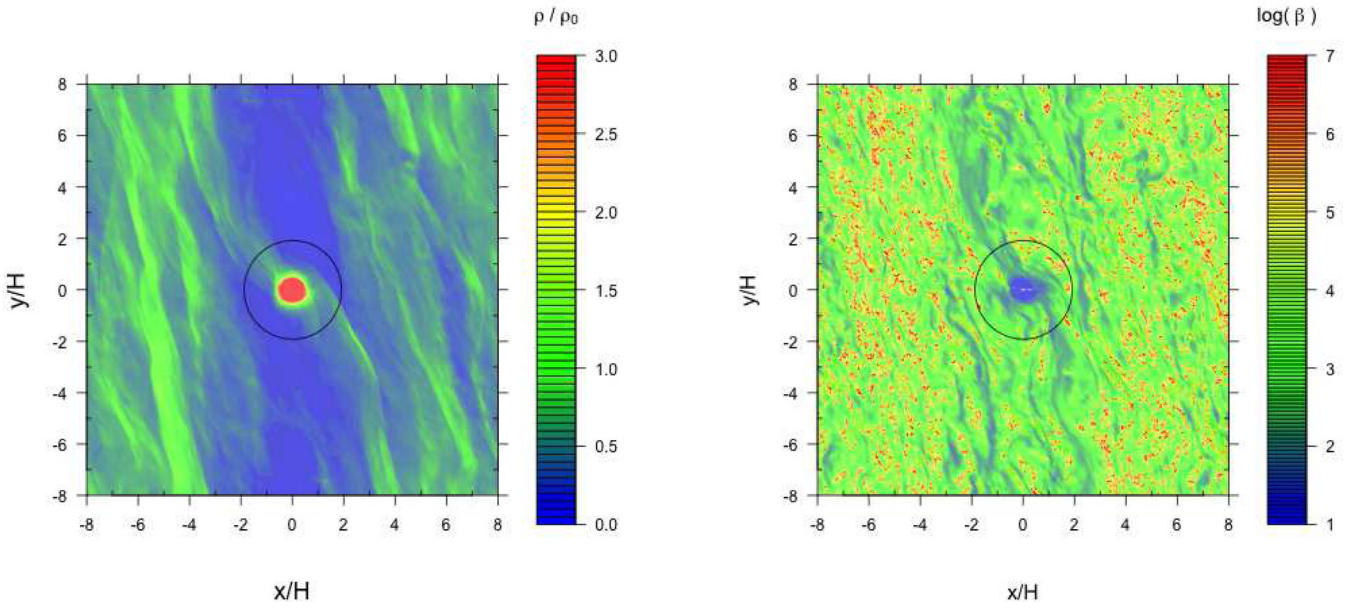

Figure 3. As in Fig. 2, but for run Z5 (planet mass $M_{\rm p} = 3.32 M_{\rm th}$).

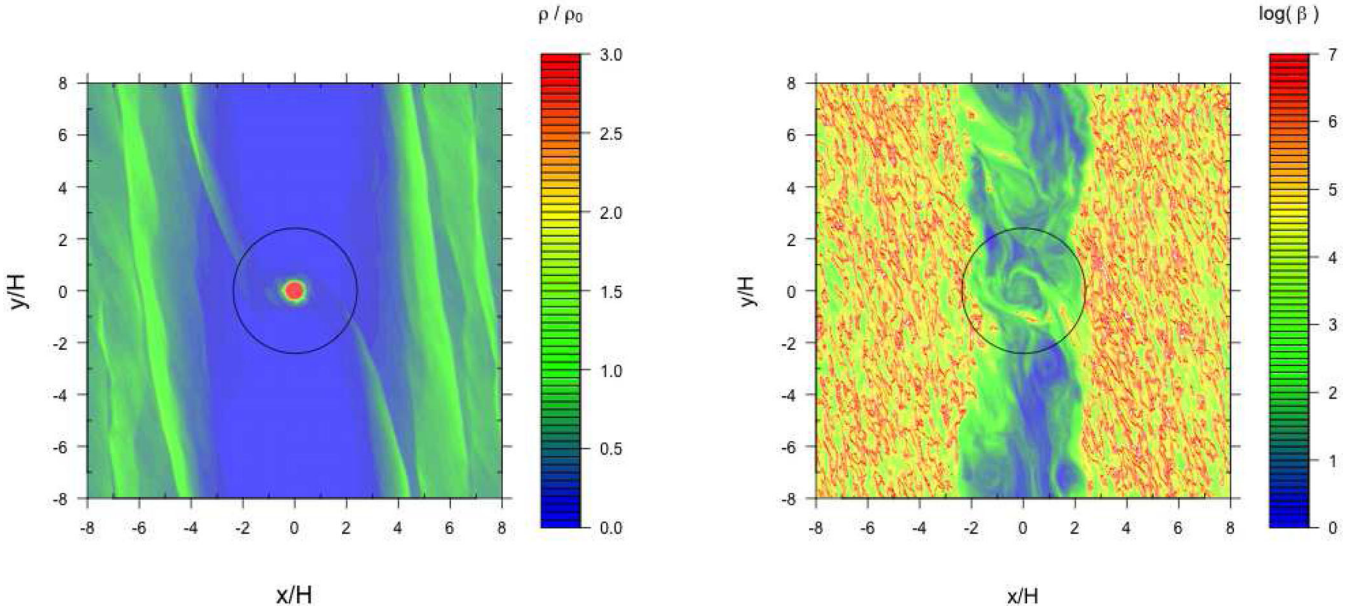

Figure 4. As in Fig. 2, but for run Z10 (planet mass $M_{\rm p} = 6.64 M_{\rm th}$).

β values are similar and slightly less than 10^3. In the instance of the low-mass planet of run YZ1 (black histogram in Fig. 8b), the lowest β values are $\sim 10^4$. There are no grid cells interior to $R_{\rm H}$ with β less than 1000 in either the Z1 or the YZ1 runs. Note that, with the exception of run Z10, β is always greater than the initial value of 400 [$\log(400) = 2.6$].

In order to determine the importance of magnetic effects at a distance of one Hill radius from each planet, the plasma β was calculated at the edge of each HS using bilinear interpolation. The mean values of the interpolated plasma β (which we denote $\bar{\beta}_{\rm H}$), as a function of planet mass, are plotted in Fig. 9. The black curve corresponds to the Z runs and the *grey* curve to the YZ runs. The error bars correspond to one standard deviation. There is a moderately decreasing trend in the case of the Z runs. For the YZ runs, we see a rather sharp drop of $\bar{\beta}_{\rm H}$ from the least massive planet ($0.66 M_{\rm th}$) to the next higher-mass planet ($1.66 M_{\rm th}$). This drop could be related to the increase in the magnitude of the mean vertical magnetic field in run YZ2 with respect to run YZ1, as can be seen in Fig. 14 (black and dark-blue curves) in Section 3.3. The value of $\bar{\beta}_{\rm H}$ decreases very slightly as planet mass increases thereafter.

3.2 Turbulent stresses

Fig. 10 shows the radial variation of the turbulent stresses, parametrized by α, for the Z runs. Stresses are averaged over the y and z directions, as well as over time. The Z run data is split across two panels in Fig. 10 to avoid clutter: the left-hand panel shows radial profiles of α for runs Z1–Z5 and the right-hand panel

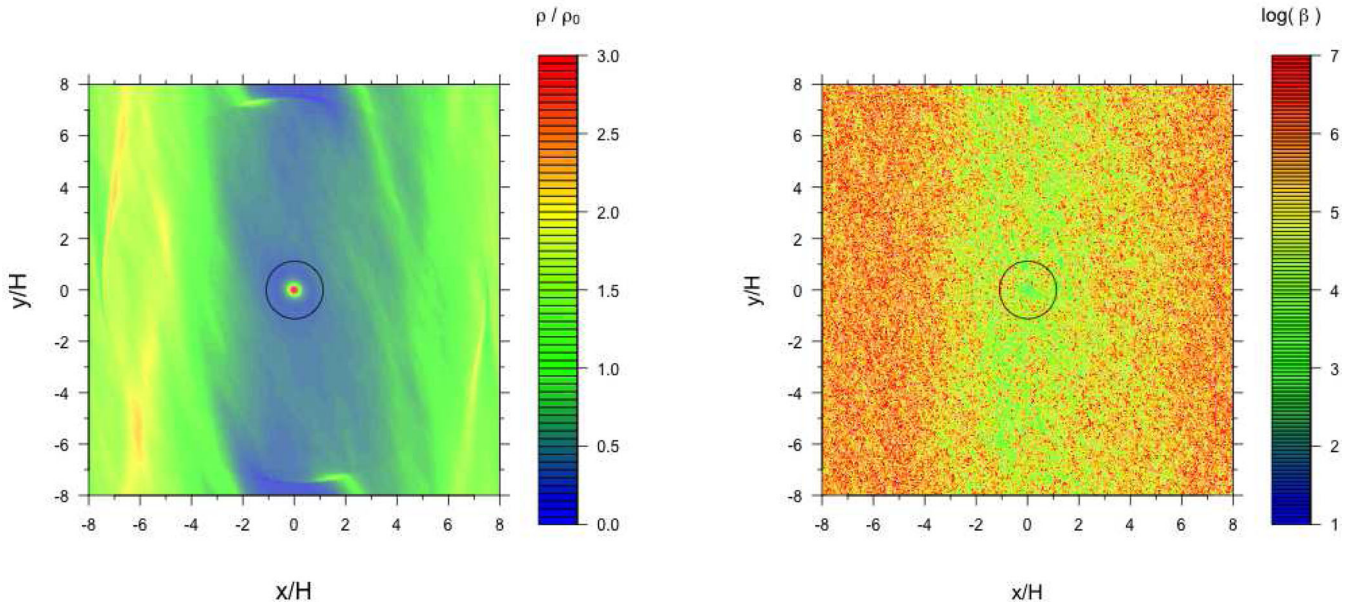

Figure 5. Time- and vertically averaged gas density (left-hand panel) and plasma β (right-hand panel) for run Z1. Values of β are generally higher than in the snapshot shown in Fig. 2 but, as in that case, most low values occur within the gap. The black circle represents the 'surface' of the planet's Hill sphere.

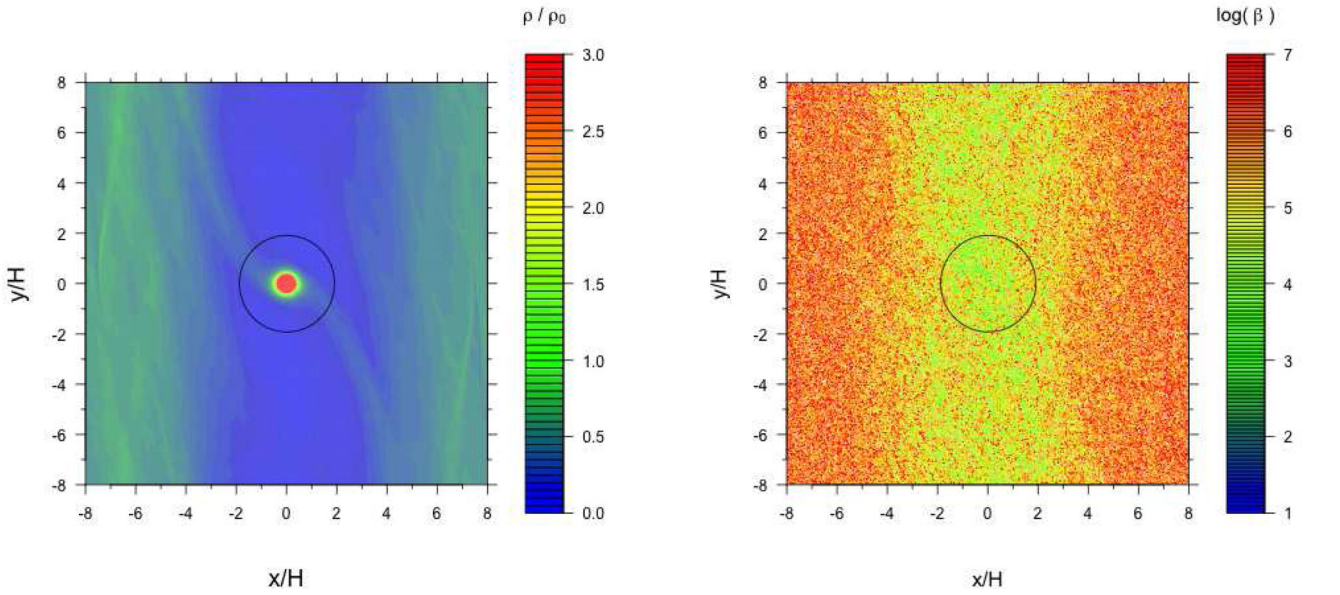

Figure 6. As in Fig. 5, but for run Z5.

for runs Z6–Z10. For planet masses $0.66M_{\rm th} < M_{\rm p} < 1.99M_{\rm th}$, α is generally larger close to the planet than away from it. As the planet mass increases, the value of α increases close to the gap edges while relatively decreasing near the planet. An analogous graph for the YZ runs is shown in Fig. 11, with qualitatively similar results to the Z runs.

The time evolution of the (y–z-averaged) magnetic part of α [$\alpha_{\rm mag} = -B_x B_y/(4\pi\rho c_s^2)$] is plotted in Fig. 12 for runs Z1, Z5 and Z10 (top, middle and bottom panels, respectively). The evolution is shown for the time periods used in the time averaging of Fig. 10. The vertical axis represents the radial direction x in the box. These data show a concentration of relatively high $\alpha_{\rm mag}$ near the box centre in the case of the least massive planet (top panel), a concentration of higher $\alpha_{\rm mag}$ values near the centre for the mid-mass planet (middle panel) and peaks of $\alpha_{\rm mag}$ away from the box radial centre for the most massive planet (bottom panel).

3.3 Vertical magnetic field

The radial profiles of the y-, z- and time-averaged vertical components of the magnetic field for the Z runs are shown in Fig. 13, where the vertical field B_z has been normalized to its initial value, B_{z0}. In the gaps created by planets with masses $0.66M_{\rm th} \lesssim M_{\rm p} \lesssim 3.32M_{\rm th}$ (left-hand panel), the magnitude of the vertical magnetic field is highest, relatively close to the planet (similar to results found by Zhu et al. 2013), and the B_z profile shows small fluctuations all along the radial extent of the box. However, for increasingly higher planet masses (right-hand panel), B_z exhibits an increasingly deeper

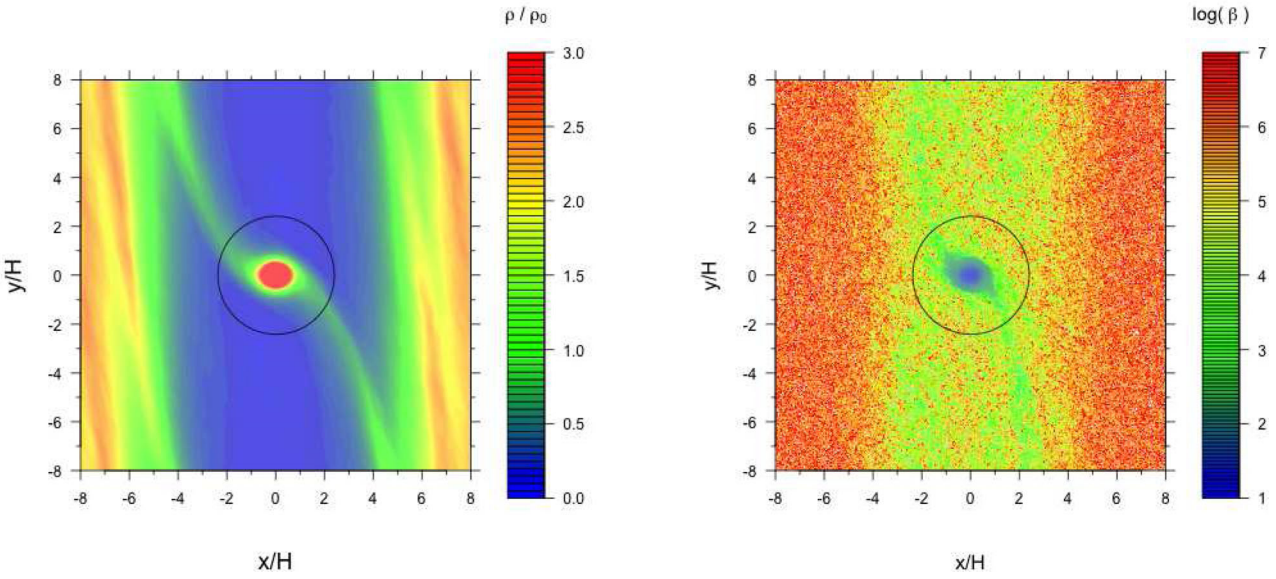

Figure 7. As in Fig. 5, but for run Z10.

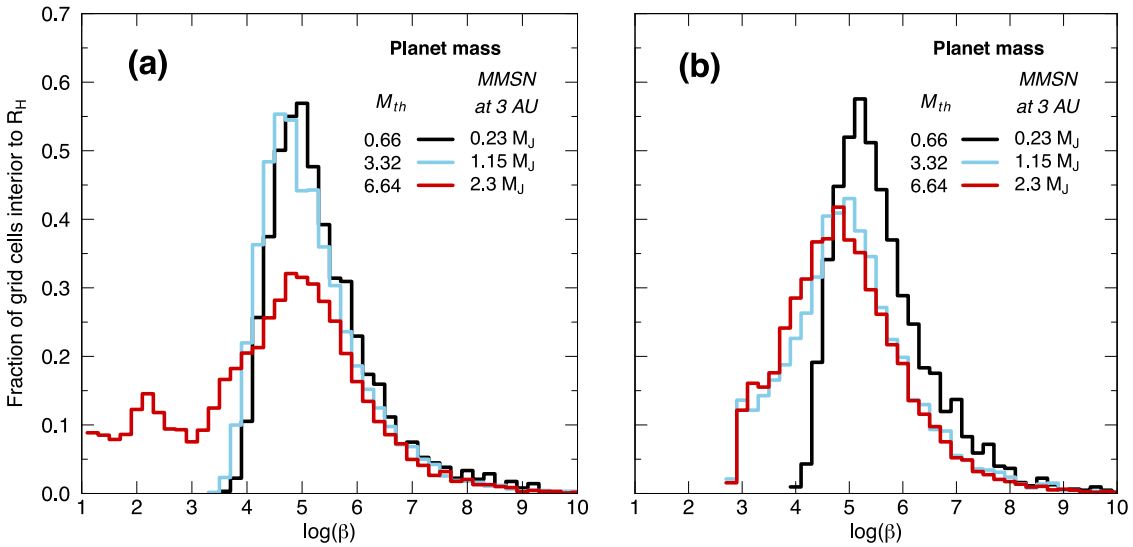

Figure 8. Time-averaged distributions of β inside the Hill sphere in runs with planet mass $0.66M_{\rm th}$ (black histograms), $3.32M_{\rm th}$ (light blue histograms) and $6.64M_{\rm th}$ (red histograms) for the case of (a) an initially uniform vertical magnetic field and (b) an initial magnetic field with both toroidal and vertical components.

trough near the planet's position. For the most massive planet, the ratio of the highest peak in B_z to the local minimum close to the gap centre is $\sim$2.

The behaviour of B_z in the YZ runs is, once again, qualitatively similar to the Z runs. As Fig. 14 shows, the field magnitude peaks near the gap centre for planet masses $0.66M_{\rm th}$ and $1.66M_{\rm th}$, approximately flattens out in that region for $M_{\rm p} = 3.32M_{\rm th}$ and develops a central trough for $M_{\rm p} = 4.98M_{\rm th}$ and $6.64M_{\rm th}$. In the latter case, the local minimum of B_z in the trough is 1.5 times smaller than the maximum close to the 'surface' of the Hill sphere.

4 DISCUSSION

In general, our results show that the strength of the vertical magnetic field, either across the gap or confined to the Hill sphere, depends on the planet mass. This raises the possibility that future observational efforts, such as high-angular resolution polarimetric observations, may one day predict the masses of gap-opening planets by, e.g. tracing the magnetic field through polarized emission of aligned aspherical dust grains (Bertrang, Flock & Wolf 2017). Currently, however, such measurements are beyond the resolution capabilities of existing instruments. See for example, a recent map of mid-infrared polarization of the disc around the Herbig Ae star AB Aurigae, obtained with the 10.4 m Gran Telescopio Canarias, which revealed a well-ordered field on a spatial scale of $\sim$50 au, corresponding to the instrumental angular resolution of 0.35 arcsec (Li et al. 2016). Such methods to infer the masses of planets capable of opening gaps could complement estimates that are based on measuring the gap width (Kanagawa et al. 2016).

We present some further comments regarding our results.

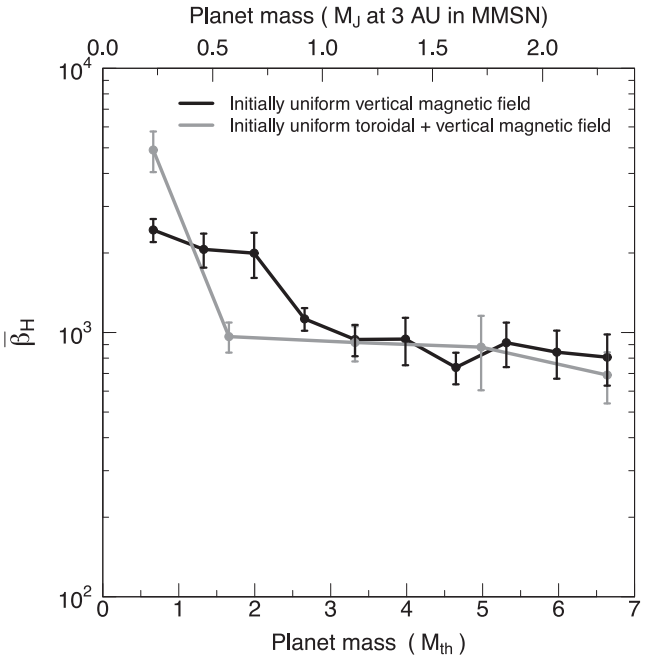

Figure 9. Mean values of the plasma β (points), which were interpolated to the perimeter of each planet's Hill sphere, as a function of planet mass. The black points represent data from the Z runs (initially uniform vertical magnetic field), while the *grey* points correspond to the YZ runs (initially uniform toroidal and vertical field). The error bars represent one standard deviation for the number of interpolated beta values around each corresponding Hill sphere's perimeter.

4.1 Plasma β

Our calculation of the plasma β at a distance of one Hill radius from each planet reveals qualitatively similar trends with planet mass for both initial magnetic field configurations, as shown in Fig. 9. For the lowest-mass planet ($M_p = 0.66M_{th}$), $\bar{\beta}_H$ is larger in the YZ calculation than in the Z calculation (by a factor of $\sim$2), meaning that the vertical field is stronger at R_H in the latter case than in the former. On the other hand, for intermediate-mass planets ($1.3M_{th} \lesssim M_p < 3.3M_{th}$), $\bar{\beta}_H$ is larger in the Z runs than in the YZ runs, corresponding to a decrease in B_z. For the rest of the planet masses ($3.3M_{th} \lesssim M_p \lesssim 6.6M_{th}$), $\bar{\beta}_H$ is similar in both Z and YZ runs.

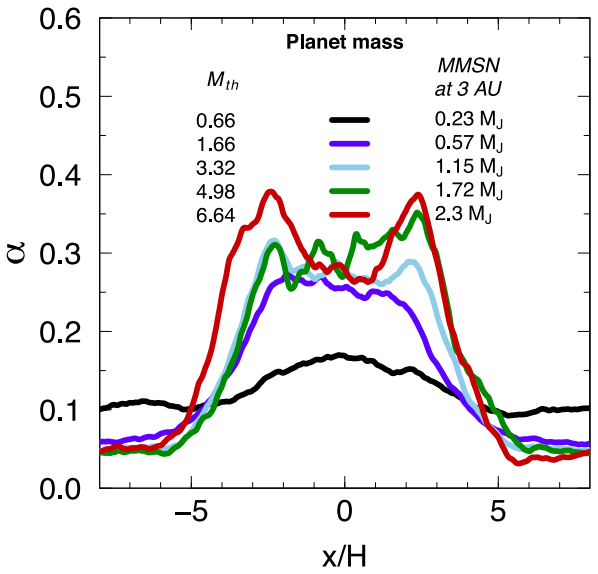

Figure 11. Similar to Fig. 10, but for the YZ runs.

4.2 Turbulent stresses

As can be seen from Figs 10 and 11, the total stresses measured by α across the different gaps are not spatially constant. This was also observed by Papaloizou et al. (2004) and Zhu et al. (2013) in simulations with an initially vertical magnetic field having a zero net flux and a non-zero net flux, respectively. In the latter work, the authors observed an increase of α inside the gap, and they attributed this increase to the efficient global transport of magnetic fields towards the gap, leading to an enhanced concentration of fields

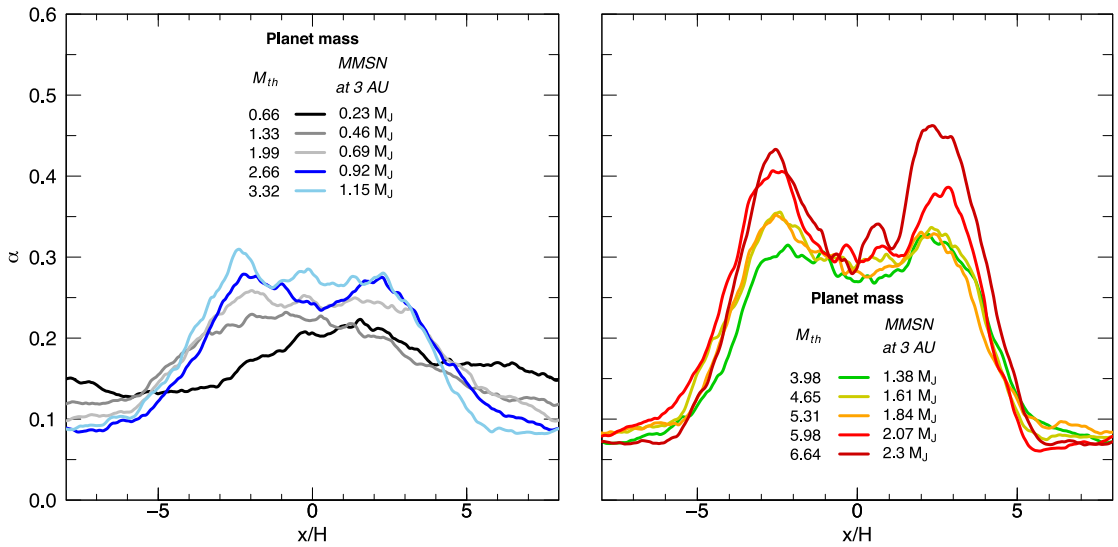

Figure 10. Azimuthally, vertically and time-averaged radial profiles of the dimensionless turbulent stresses α, given by Eq. (5), for the Z runs. For clarity, data have been split into two panels: the left-hand panel shows data for runs Z1–Z5 and the right-hand panel for runs Z6–Z10. Values of α are higher close to the gap edges than at the gap centre, as the planet mass increases.

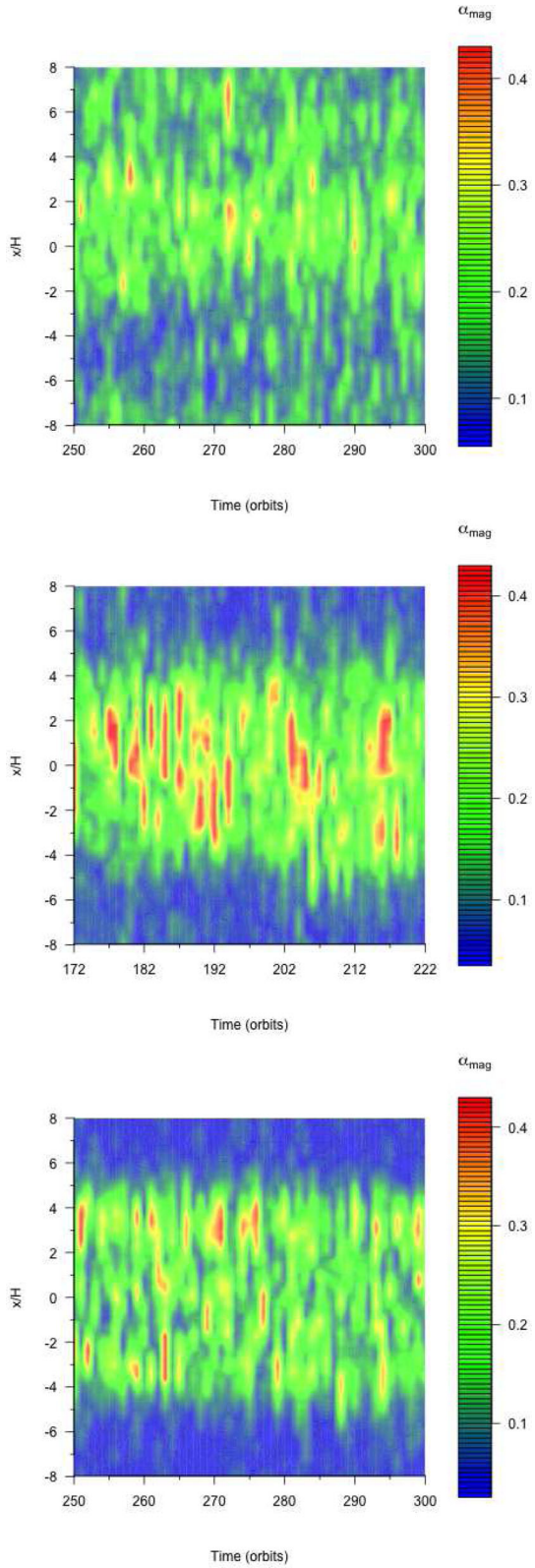

Figure 12. Space–time values of α_{mag}, the magnetic part of the dimensionless turbulent stress for runs Z1 (top panel), Z5 (middle panel) and Z10 (bottom panel). Peaks in α_{mag} move away from the radial box centre, $x = 0$, for higher planet mass.

with respect to the gas density. This interpretation seems to be consistent with our results, in which B_z is higher near the gap centre than near the gap edges for low-mass planets ($M_p \lesssim 3M_{th}$; Figs 13 and 14). Conversely, our data for massive planets ($M_p \gtrsim 4M_{th}$) show a decrease of α when B_z dips towards the gap centre. In summary, the behaviour of the turbulence intensity across the gaps may be mirroring the strength of the vertical magnetic field, also across the gaps.

4.3 Vertical magnetic field

We have corroborated previous studies that indicate an increase in magnetic field strength inside a gap opened by a planet in a protoplanetary disc, with respect to the field strength outside the gap (Papaloizou et al. 2004; Zhu et al. 2013; Keith & Wardle 2015). However, our results reveal a slightly more complex structure of the field than suggested by the earlier work. Specifically, we find that, for planet masses $\gtrsim 4M_{th}$, the radial profile of B_z develops two peaks at either side of the planet, with a local minimum in the near vicinity of the planet. If the planet mass is less than $\sim 4M_{th}$, B_z peaks towards the centre of the gap (Figs 13 and 14), as found by Zhu et al. (2013) for $M_p = 1M_{th}$ (their fig. 8). This behaviour occurs for both of our initial field configurations.

The different magnitudes of B_z across the planet-induced gaps have implications for the circumplanetary MHD flow. Gas flowing into the gap and into the Hill sphere would carry along magnetic fields, providing a certain degree of magnetization to the circumplanetary disc. These gap magnetic fields could play a role in launching magnetocentrifugally driven outflows, as observed in a global PPD simulation (Gressel et al. 2013). For example, rotation of the CPD would generate a helical **B** field that would lead to the collimation of a jet (although a magnetocentrifugal origin of the observed numerical outflow is still speculative). However, a deficiency of vertical fields in the vicinity of the CPD could lead to unfavourable conditions for jet launching. Likewise, if the vertical field strength varies across the gap, the corresponding variation of magnetic torques may produce different local conditions for the generation of magnetocentrifugal winds. These winds require strong enough fields to act as 'rigid wires' (Turner et al. 2014), but if the field strength diminishes considerably around a massive planet, such winds might not be generated above those locations.

4.4 Future work

Non-ideal MHD effects would play a significant role in determining the magnetic field structure inside a gap surrounding planets. The magnetic coupling between the field and the gas is determined by the transport coefficients for Ohmic resistivity (which is mainly due to electron–neutral collisions), ambipolar diffusion (arising from ion–neutral drift) and the Hall effect (due to electron–ion drift). These effects would cause the GMF to diffuse through the gas at different rates, depending on the relative strength of the coefficients. The semi-analytical calculations of Keith & Wardle (2015) showed that the Hall effect is particularly important in establishing the field configuration, as well as the flow regime, in the gap. The Hall effect is strong at altitudes less than two scaleheights from the disc midplane, and it could actually lead to the development of MRI, even if Ohmic resistivity and ambipolar diffusion are strong. Keith & Wardle (2015) found that a gap opened by a Jupiter-mass planet would be unstable to the MRI if the vertical magnetic field was parallel to the disc's rotation axis. On the other hand, if the vertical field and the rotation axis were anti-parallel, Hall drift would act

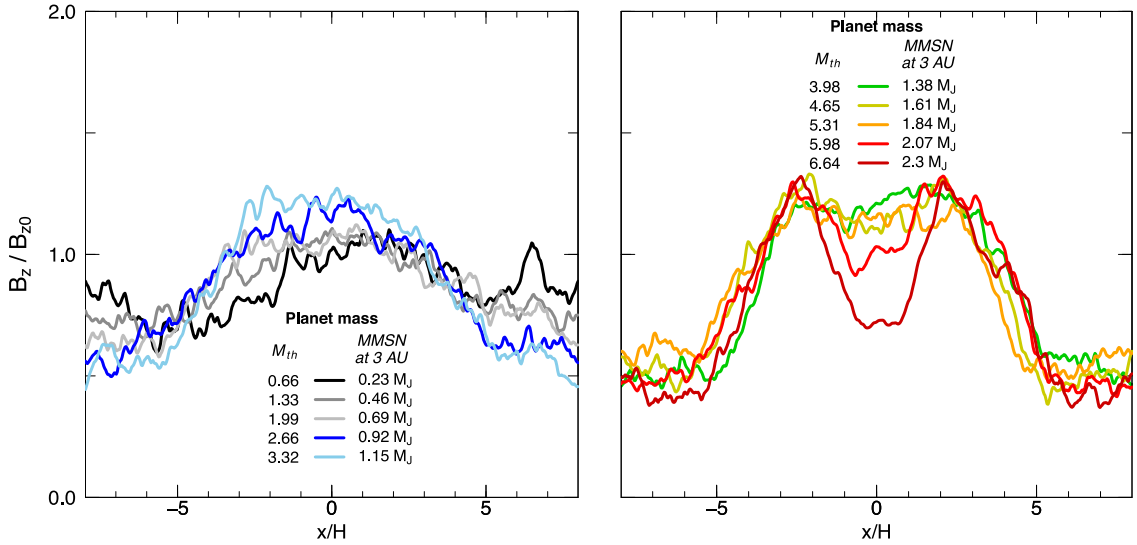

Figure 13. Azimuthally, vertically and time-averaged radial profiles of the vertical magnetic field B_z, normalized by its initial value B_{z0}, for the Z runs. The magnitude of B_z shows a dip near the gap center for planet masses $M_p > 3.32 M_{th}$.

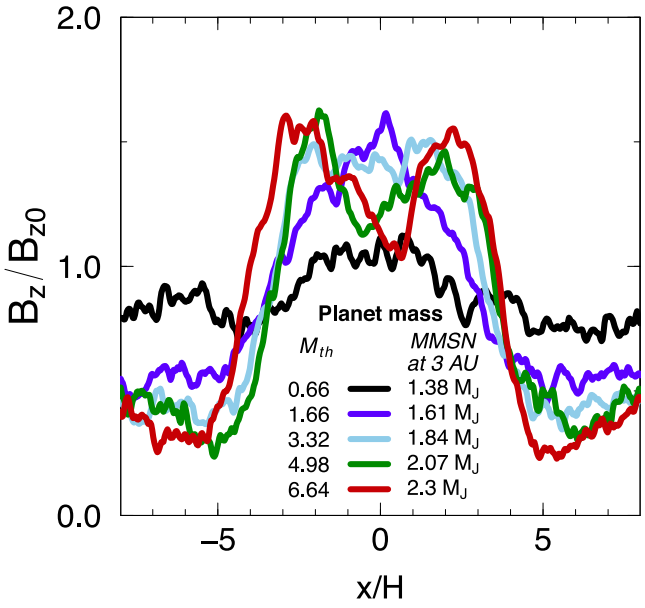

Figure 14. Similar to Fig. 13, but for the YZ runs. The magnitude of B_z shows a dip near the gap center for planet masses $M_p > 3.32 M_{th}$.

against Keplerian shear (which is harnessed by the MRI dynamo to generate turbulence) and the gap would be non-turbulent. A complete picture of GMF evolution, then, requires incorporation of these non-ideal effects into numerical models.

A further improvement on our models will be to include the vertical variation of the gas density, up to a few disc scaleheights above the mid-plane. This variation will be reflected in the gap structure, turbulence intensity and GMF magnitude. In the latter case, the resistive-MHD study of Keith & Wardle (2015) found that the largest contribution to the GMF below $\sim 2H$ is due to a magnetic field component produced by MRI turbulence. This component is present only below $2H$. Above that height, vertical and toroidal components are present, with the toroidal component dominating over the vertical one up to a height of $\sim 4H$. Above $4H$, the magnitude of the vertical magnetic field is larger than that of the toroidal field.

There remains the possibility that the "M" shapes of the radial profiles of the magnetic field seen for the more massive planets depend on the box height (even without vertical stratification of the gas density). However, two short simulations performed with a slightly taller box ($1.2H$) and slightly different numerical resolutions (32 and 26 grid cells per scale height), with the largest planet mass, and with a purely vertical initial magnetic field, showed a qualitatively similar magnetic profile to the one in run Z10 shown in Fig. 13. Naturally, a full study of the dependence of the GMF geometry on box size and initial magnetic flux is required, preferably with a variety of numerical codes.

5 CONCLUSIONS

We have numerically calculated values of the vertical magnetic field (B_z) threading gaps opened by planets of various masses in a turbulent protoplanetary disc. In order to focus on a local region surrounding a gap-opening planet, we employed the shearing box approximation of a rotating astrophysical system. To this end, we used the grid-based, MHD code ATHENA. Ideal MHD was assumed for our calculations, an assumption that is justified by recent studies (Gressel et al. 2013; Keith & Wardle 2015) indicating that MRI activity in the gap region could develop under certain conditions.

Our models extend the parameter space of planet mass with respect to the work of Zhu et al. (2013): We studied gap opening by planets of masses between 0.66 and 6.64 thermal masses (M_{th}). These models also provide a comparison between two different initial magnetic field configurations: one in which the initial field has a uniform, vertical component only ('Z' configuration) and another one in which the field has both toroidal and vertical components ('YZ' configuration). Despite the difference in initial magnetic field configuration, the radial distribution of the vertical magnetic field across the gap is qualitatively similar in both cases.

Our results corroborate prior findings regarding the larger strength of the (y-, z- and time-averaged) vertical magnetic field inside the gap than outside for low-mass planets. Measurements of the distribution of β within the Hill sphere of three planets of

different masses (0.66, 3.32 and 6.64$M_{\rm th}$) indicate that, in the case of medium- and large-sized planets in the YZ initial magnetic field configuration, the interior of their Hill spheres contains more low-β values (high B_z) than the Hill sphere of the smallest planet. For the Z configuration, only the most massive planet contains very low-β values (10–10^2) in its Hill sphere.

The structure of the radial profiles of B_z across the different gaps also depends on the planet mass, and very little on the initial magnetic field configuration. For both configurations, the less massive planets generate a radial profile that *peaks* close to the gap centre, while the more massive planets generate profiles that *dip* at the gap centre. The ratio of peak-to-dip for the largest planet in both types of runs is between 1.5 and 2. Further improvements to these calculations could aid future observational determinations of planet masses performed through high-resolution polarimetry.

We interpolated the values of β to the edge of the various Hill spheres, and the mean of those interpolated values ($\bar{\beta}_{\rm H}$) was plotted as a function of planet mass, for the two initial magnetic field configurations. In the case of the Z configuration, $\bar{\beta}_{\rm H}$ decreases moderately with the planet mass. In the case of the YZ configuration, $\bar{\beta}_{\rm H}$ shows a somewhat abrupt decrease from the smallest to the second-smallest planet, and a very small decrease for larger planet masses.

Future work should take into account the role of ambipolar diffusion, Ohmic and Hall resistivities, the vertical variation of gas density, and different box heights and initial magnetic field configurations.

ACKNOWLEDGEMENTS

Comments by an anonymous referee helped in clarifying several points of the original manuscript. The authors acknowledge the Texas Advanced Computing Center (TACC) at The University of Texas at Austin for providing HPC resources that have contributed to the research results reported within this paper (URL: http://www.tacc.utexas.edu).

REFERENCES

Akiyama E. et al., 2015, ApJ, 802, 17
ALMA Partnership et al., 2015, ApJL, 808, L3
Andrews S. M. et al., 2016, ApJ, 820, L40
Armitage P. J., 2015, preprint (arXiv:1509.06382)
Balbus S. A., Hawley J. F., 1998, Rev. Mod. Phys., 70, 1
Bertrang G. H.-M., Flock M., Wolf S., 2017, MNRAS, 464, L61
Carballido A., Matthews L. S., Hyde T. W., 2016, ApJ, 823, 80
Dong R., Rafikov R. R., Stone J. M., Petrovich C., 2011, ApJ, 741, 56
Fujii Y. I., Okuzumi S., Tanigawa T., Inutsuka S., 2014, ApJ, 785, 101
Fung J., Chiang E., 2016, ApJ, 832, 105
Gressel O., Nelson R. P., Turner N. J., Ziegler U., 2013, ApJ, 779, 59
Hawley J. F., Gammie C. F., Balbus S. A., 1995, ApJ, 440, 742
Hayashi C., 1981, Prog. Theor. Phys. Suppl., 70, 35
Kanagawa K D., Muto T., Tanaka H., Tanigawa T., Takeuchi T., Tsukagoshi T., Momose M., 2016, PASJ, 68, 43
Keith S. L., Wardle M., 2014, MNRAS, 440, 89
Keith S. L., Wardle M., 2015, MNRAS, 451, 1104.
Kley W., Nelson R. P., 2012, ARA&A, 50, 211
Li D., Pantin E., Telesco C. M., Zhang H., Wright C. M., Barnes P. J., Packham C., Marinãs N., 2016, ApJ, 832, 18
Lin D. N. C., Papaloizou J., 1986, ApJ, 309, 846
Papaloizou J. C. B., Nelson R. P., Snellgrove M., 2004, MNRAS, 350, 829
Rafikov R. R., 2006, ApJ, 648, 666
Shakura N. I., Sunyaev R. A., 1973, A&A, 24, 337
Stone J. M., Gardiner T. A., Teuben P., Hawley J. F., Simon J. B., 2008, ApJS, 178, 137
Tanigawa T., Ohtsuki K., Machida M., 2012, ApJ, 747, 47
Turner N. J., Fromang S., Gammie C., Klahr H., Lesur G., Wardle M., Bai X.-N., 2014, in Beuther H., Klessen R., Dullemond C. P., Henning Th., eds, Protostars and Planets VI. Univ. Arizona Press, Tucson, p. 411
van Boekel R. et al., 2017, ApJ, 837, 132
Zhu Z., Stone J. M., Rafikov R. R., 2013, ApJ, 768, 143

This paper has been typeset from a TEX/LATEX file prepared by the author.